1	2		
	First Displaced Vertex Seerah for Floatroppeduced Strongly Internating Massive		
3	First Displaced Vertex Search for Electroproduced Strongly Interacting Massive		
4	Particles by the HPS Experiment		
5	(HPS Collaboration)		
	P. H. Adrian, C. Bravo,* P. Butti, M. Diamond, C. Field, N. Graf, M. Graham,† R. Herbst, J. Jaros,		
6	T. Maruyama, J. McCormick, T. Nelson, A. Odian, M. Oriunno, B. Reese, M. Solt, and S. Uemura		
7 8	SLAC National Accelerator Laboratory, Stanford University, Stanford, CA 94309, USA		
9	N. A. Baltzell, S. Boyarinov, V. D. Burkert, C. Cuevas, A. Deur, H. Egiyan, L. Elouadrhiri, A. Freyberger,		
10	F. X. Girod, V. Kubarovsky, B. Raydo, Y. G. Sharabian, S. Stepanyan, M. Ungaro, and B. Wojtsekhowski		
11	Thomas Jefferson National Accelerator Facility, Newport News, Virginia 23606, USA		
12	M. Battaglieri, A. Celentano, R. De Vita, L. Marsicano, and M. Osipenko		
13	INFN, Sezione di Genova, 16146 Genova, Italy		
14	M. Bondí, M. De Napoli, E. Leonora, and N. Randazzo		
15	INFN, Sezione di Catania, 95123 Catania, Italy		
16	S. Bueltmann, G. Kalicy, and L. B. Weinstein		
17	Old Dominion University, Norfolk, Virginia 23529, USA		
18	D. Calvo and A. Filippi		
19	INFN, Sezione di Torino, 10125 Torino, Italy		
20	T. Cao, B. Crowe, M. Holtrop, and S. McCarty		
21	University of New Hampshire, Durham, New Hampshire 03824, USA		
22	M. Carpinelli		
23	INFN, Laboratori Nazionali del Sud, 95123 Catania, Italy and		
24	University di Milano Bicocca, 20126 Milano, Italy		
25	G. Charles, R. Dupre, M. Guidal, C. Munoz Camacho, S. Niccolai, and A. Simonyan		
26	Université Paris-Saclay, CNRS, IJCLab, 91405, Orsay, France		
27	L. Colaneri, A. D'Angelo, and A. Rizzo		
28	Università di Roma Tor Vergata, 00133 Rome Italy and		
29	INFN, Sezione di Roma Tor Vergata, 00133 Rome, Italy		
30	W. Cooper		
31	Fermi National Accelerator Laboratory, Batavia, IL 60510, USA		
32	N. Dashyan, N. Gevorgyan, and H. Voskanyan		
33	Yerevan Physics Institute, 375036 Yerevan, Armenia		
24	R. Essig		
34 35	C. N. Yang Institute for Theoretical Physics, Stony Brook University, Stony Brook, NY 11794, USA		
36	V. Fadeyev, A. Grillo, R. P. Johnson, and A. Spellman		
37	Santa Cruz Institute for Particle Physics, University of California, Santa Cruz, CA 95064, USA		
38	M. Garçon		
39	IRFU, CEA, Université Paris-Saclay, F-91190 Gif-sur-Yvette, France		
40	K. A. Griffioen and S. Paul		
41	College of William & Mary, Williamsburg, Virginia 23187, USA		

M. Khandaker Idaho State University, Pocatello, ID, 83209, USA

K. Livingston, B. McKinnon, K. Moffeit, and D. Sokhan University of Glasgow, Glasgow G12 8QQ, United Kingdom

O. Moreno

SLAC National Accelerator Laboratory, Stanford University, Stanford, CA 94309, USA and Santa Cruz Institute for Particle Physics, University of California, Santa Cruz, CA 95064, USA

R. Paremuzyan

Thomas Jefferson National Accelerator Facility, Newport News, Virginia 23606, USA and University of New Hampshire, Durham, New Hampshire 03824, USA

P. Schuster and N. Toro

SLAC National Accelerator Laboratory, Stanford University, Stanford, CA 94309, USA and Perimeter Institute, Ontario, Canada N2L 2Y5

G. Simi

Università di Padova, 35122 Padova, Italy and INFN, Sezione di Padova, 16146 Padova, Italy

V. Sipala

Università di Sassari, 07100 Sassari, Italy and INFN, Laboratori Nazionali del Sud, 95123 Catania, Italy

H. Szumila-Vance

Thomas Jefferson National Accelerator Facility, Newport News, Virginia 23606, USA and Old Dominion University, Norfolk, Virginia 23529, USA

T. Eichlersmith

University of Minnesota, Minneapolis, MN 55455, USA

L. Tompkins, S. Gaiser, E. Peets, and R. O'Dwyer Stanford University, Stanford, CA 94305 (Dated: September 24, 2025)

The Heavy Photon Search experiment (HPS) is a fixed-target electron beam experiment designed to search for e^+e^- mass resonances and displaced decays using a forward acceptance spectrometer. In this paper, we report on a search for naturally long-lived "dark" vector mesons (V_D) arising from a Hidden Sector of beyond-Standard-Model strongly interacting massive particles (SIMPs), characterized by a QCD-like $SU(3)_D$ symmetry and coupled to the Standard Model photon via a new $U(1)_D$ gauge interaction mediated by the "heavy photon", or A'. The results are based on an integrated luminosity of $10\,608\,\mathrm{nb}^{-1}$ collected during the 2016 HPS Engineering Run. The displaced vertex search for $V_D \to e^+e^-$ in the e^+e^- invariant mass range $39\,\mathrm{MeV}$ – $179\,\mathrm{MeV}$ showed no evidence for signal above the QED background.

I. INTRODUCTION

In recent years, a number of extensions to the Standard ⁸⁷ Model (SM) have been proposed which include new gauge ⁸⁸ symmetries that allow for so-called dark sectors with in- ⁸⁹ direct coupling to SM to account for the dark matter. ⁹⁰ In the simplest of these, a new $U(1)_D$ gauge field is in- ⁹¹ troduced in the hidden sector, giving rise to a poten-

 * Corresponding Author: bravo@slac.stanford.edu

42

43

52

53

62

65

69

70

71

82

tially massive spin-1 vector gauge boson referred to as the "dark photon", or A'. The dark photon kinetically mixes with the SM photon through a massive charged fermion loop, a process that is often simplified to an effective coupling with strength ϵ . This coupling enables the electroproduction of dark photons through a bremsstrahlung-like process on a nuclear target, as illustrated in Figure 1.

The final state signatures from the dark photon decay depend on the structure of the hidden sector. Our previous analyses [1, 2] were optimized to search for an A' in the simplest case where the A', being light compared to other dark states, can only decay back into SM

[†] Corresponding Author: mgraham@slac.stanford.edu

leptons. There are a number of other models in the liter-125 ature, some of which will give different signatures in the 126 Heavy Photon Search experiment (HPS) detector. In this 127 work, we present a search for particles predicted by the 128 SIMP model [3, 4]. In Section II, this paper discusses 129 the SIMP model, highlighting both theoretical and ex-130 perimental constraints. This is followed by brief descrip-131 tions of the HPS setup in Section III, and the data col-132 lection and reconstruction in Section IV. Section V and 133 Section VI detail the event selection and data analysis, 134 respectively. Section VII summarizes the findings and 135 suggests possible improvements in future analyses.

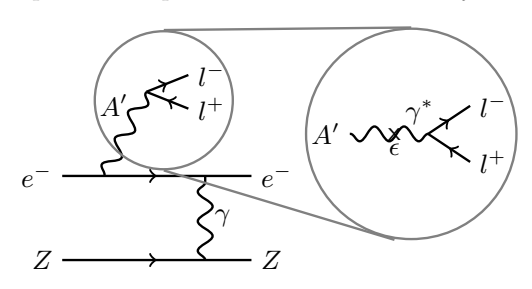


FIG. 1. Electro-production of A' through a bremsstrahlung-like process and subsequent visible leptonic decay. The inset¹⁴⁷ highlights the conversion of dark photons to SM γ through₁₄₈ kinetic mixing with strength ϵ .

II. SIMP MODEL AND PARAMETER CONSTRAINTS

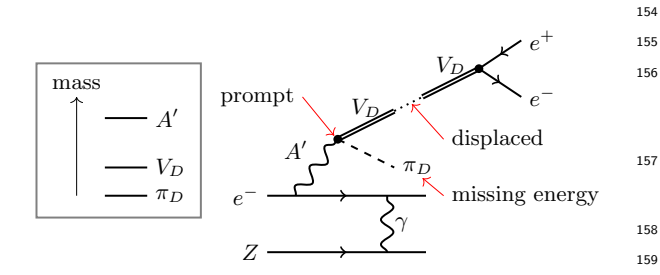


FIG. 2. Production of e^+e^- from the decay of a dark vector₁₆₁ meson V_D via a virtual dark photon A'.

In contrast to the minimal dark photon model, where ¹⁶⁴ thermal freeze-out is achieved through $2 \rightarrow 2$ annihilation ¹⁶⁵ into SM particles, extended dark sector models permit al-¹⁶⁶ ternative freeze-out mechanisms. Introducing QCD-like ¹⁶⁷ $SU(3)_D$ gauge symmetries in the hidden sector gives rise ¹⁶⁸ to strongly interacting massive particles, namely dark pi-¹⁶⁹ ons (π_D) and dark vector mesons (V_D) , where the lightest ¹⁷⁰ states, the dark pions, serve as dark matter candidates. ¹⁷¹

While these models still require kinetic equilibration¹⁷² with the SM, dark pion self-interactions allow for an ad-¹⁷³ ditional $3\pi_D \rightarrow 2\pi_D$ annihilation process that depletes¹⁷⁴ the dark matter relic density even after decoupling from¹⁷⁵ the SM [3]. The inclusion of V_D further enables a semi-¹⁷⁶ annihilation channel, $\pi_D\pi_D \rightarrow \pi_D V_D$, followed by the¹⁷⁷

decay $V_D \to SM$ through a virtual A'. This decay can produce a displaced e^+e^- pair, a signature well matched to the HPS detector's capabilities [5], as illustrated in Figure 2.

The SIMP model considered in this paper involves six parameters: the dark photon, dark pion, and dark vector masses, $m_{A'}$, m_{π_D} , and m_{V_D} , respectively; the A' kinetic mixing strength ϵ with the SM photon; the hidden sector $U(1)_D$ gauge coupling constant α_D ; and finally, the ratio of the dark pion mass to the dark pion decay constant m_{π_D}/f_{π_D} . These parameters are constrained by both theoretical consistency and experimental requirements. Perturbativity demands $\alpha_D < 1$, and we fix $\alpha_D = 10^{-2}$ in this work. This implies $m_{\pi_D}/f_{\pi_D} \lesssim 4\pi$, since $m_{\pi_D}/f_{\pi_D} \sim g_D \sim 4\pi\alpha_D$. The kinetic mixing parameter must fall within $10^{-6} < \epsilon < 10^{-2}$ [6]. Values of $\epsilon \gtrsim 10^{-2}$ suppress semi-annihilation, while $\epsilon \lesssim 10^{-6}$ fail to maintain kinetic equilibrium between the dark and visible sectors [5].

We search the parameter space for decays that are visible and reconstructible in the HPS detector; this yields constraints on our search:

- $m_{A'} > 2m_{\pi_D}$ to suppress $\pi\pi \to A'\pi$
- $m_{A'} > m_{\pi_D} + m_{V_D}$ to allow $A' \to \pi_D V_D$
- $m_{A'} < 2m_{\mu}$ and $m_{A'} < 2m_{V_D}$ to favor decays with good acceptance in our detector
- $m_{V_D} < 2m_{\pi_D}$ to prevent $V_D \to \pi_D \pi_D$ and ensure visible decay

To manage the complexity of the parameter space, we adopt an often-cited benchmark model with fixed mass ratios. The search is then performed as a function of $m_{A'}$ and ϵ , for the representative value of $m_{\pi_D}/f_{\pi_D}=4\pi$.

III. THE HPS EXPERIMENT

Although the HPS detector was designed to search for prompt and displaced A', it is also sensitive to a subset of SIMP decays, which can produce similar e^+e^- final states but with different kinematics. This section provides an overview of the Continuous Electron Beam Accelerator Facility (CEBAF) accelerator and the HPS detector. More detailed information can be found in an earlier HPS publication [1].

HPS uses the electron beam from the CEBAF [7] at Thomas Jefferson National Accelerator Facility in Newport News, Virginia. CEBAF's ability to provide a high-repetition-rate, multi-GeV electron beam with low per-bunch charge is essential to HPS, allowing for high-luminosity operation with minimal pile-up and manageable detector occupancies.

HPS targets rare e^+e^- decays while rejecting large QED backgrounds. This requires a precise measurement of the invariant mass and the position of the decay vertex. The overall geometry of the detector is optimized for boosted forward-going e^+e^- pairs, a characteristic shared

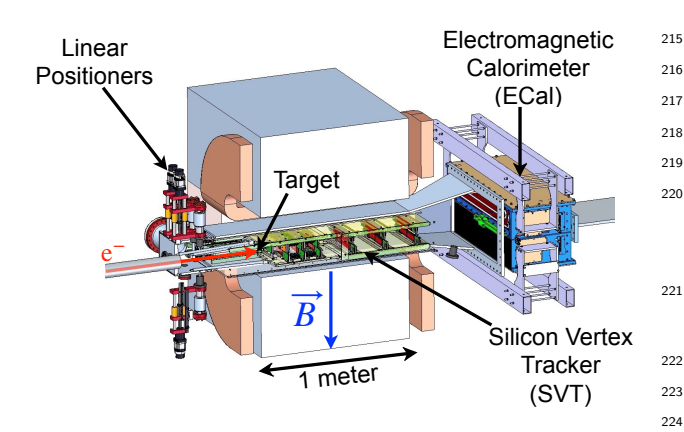


FIG. 3. A cutaway view of the HPS detector showing the ²²⁵ SVT in a vacuum chamber inside the bore of the spectrometer ²²⁶ magnet and the downstream ECal. The positions of the target ²²⁷ and the front portions of the SVT are controlled by a set of ²²⁸ linear positioning motors upstream of the detector. ²²⁹

by many potential signals, including both A' and SIMP²³² decays. In the nominal A' scenario, the signal (and hence the e^+e^- pair) carries nearly all the beam energy, peak-²³⁴ ing at $x = E_{A'}/E_{\rm beam} \rightarrow 1$ [6]. In contrast, for the SIMP²³⁵ model, the A' decays to dark-sector particles that may²³⁶ then decay to e^+e^- . This results in lower x for the pair²³⁷ and a less boosted decay with wider opening angles [5].²³⁸ Although HPS has limited acceptance for such events, it ²³⁹ remains sensitive in regions where the SIMP decay prod-²⁴⁰ ucts still fall within the detector's forward coverage.

178

179

180

181

182

183

185

186

188

189

190

191

192

194

195

196

197

198

199

201

202

203

204

205

207

208

210

211

212

213

To produce forward e^+e^- pairs, HPS places a thin 242 (4 µm) tungsten foil target and Silicon Vertex Tracker (SVT) inside a dipole magnet. The magnetic field, $0.5 \, \mathrm{T}^{244}$ for the 2016 run, bends charged particles in the horizontal "beam plane", separating electron from positron tracks and lower momentum signal tracks from beamrelated backgrounds, mostly full-energy electrons or very low-momentum charged particles from the target.

The SVT is split into upper and lower halves, posi- $_{251}$ tioned just above and below the beam plane, to maximize $_{252}$ acceptance near the beam while avoiding the large rate $_{253}$ of scattered beam electrons. The SVT halves are placed $_{254}$ at a vertical angle of approximately $\pm 15\,\mathrm{mrad}$ from the beam plane. Each SVT half includes six modules of axial/stereo sensor pairs, arranged from 10 to 90 cm downstream of the target. Each sensor has a 60 μ m readout strip pitch.

The Electromagnatic Calorimeter (ECal) sits downstream of the spectrometer. It is composed of 442 PbWO₄ crystals arranged in two identical arrays above and below the beam plane. The ECal serves two roles in the HPS experiment. First, it is used in the fast $e^+e^$ trigger system, selecting events that have two clusters in opposite quadrants of the ECal, i.e. in the top right and bottom left of the ECal or vice versa. A detailed description of this trigger setup, referred to as Pair1 trigger, is²⁵⁵ given in [1]. Second, it is used in particle reconstruction²⁵⁶ where we match the SVT track to an ECal cluster helping to reduce background events from mis-reconstructed and out-of-time tracks.

The key components of the HPS apparatus are shown in Figure 3. More detailed motivations and detector specifications are discussed in [1].

IV. DATA AND RECONSTRUCTION

The results presented here use data collected during the 2016 Engineering Run. All data used for analysis were collected at a beam energy of 2.3 GeV with a current of 200 nA on a tungsten foil target $4\,\mu\mathrm{m}~(\approx\!0.125\%~X_0)$ thick. The total luminosity of this dataset is $10\,608\,\mathrm{nb}^{-1}$, comprising 7.2 billion triggered events from a total charge on target of 67.2 mC. In addition to physics runs, a number of special runs were taken, such as field-off runs and runs with a trigger dedicated to collecting scattered single electrons over a wide range of scattering angles. Data from these runs were used to calibrate and align the ECal and SVT.

In addition to experimental data, the analysis presented here makes use of Monte Carlo (MC) simulations to understand some attributes of the signal and background. MadGraph5 [8] is used to generate signal samples at a range of masses, as well as background samples. These backgrounds include both Bethe-Heitler and radiative tridents, see Figure 4, and their interference term, and wide-angle Bremsstrahlung (WAB) events. These are the relevant background samples since the trident processes and converted WAB events, where the photon undergoes e^+e^- pair production, have the same final state as the dark vector decay that we are interested in. Møller scattering events are also used to study the mass resolution. The beam backgrounds, predominantly scattered single electrons, are simulated using EGS5 [9] and overlaid on all MC samples, distributed according to the time structure of the beam to account for pileup effects. The simulation of generated samples uses Geant4 [10] to model interactions with the detector, after which the detector response simulation and reconstruction are performed.

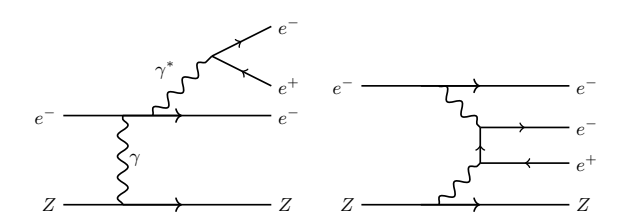


FIG. 4. Radiative (left) and Bethe-Heitler tridents (right) have the same final state particles as the e^+e^- production from a dark vector decay shown in Figure 2.

The event reconstruction follows the procedure detailed in [1]. Briefly, energy deposits in the ECal are

grouped into clusters, with per-crystal energy corrections applied using calibration tables. These clusters are constructed by grouping high amplitude seed hits (found with a scan for above threshold hits) with their viable nearest and next-to-nearest neighbors. This simple process is followed by a common hit removal stage, and the cluster energy is then defined as the sum of energies of its constituent hits.

In the SVT, tracks are reconstructed using a combinatorial Kalman filter both track finding and fitting and incorporates multiple scattering. Each track is then propagated to the ECal and matched to an ECal cluster. A matched track-cluster pair is referred to as a reconstructed particle.

Pairs of oppositely charged reconstructed particles, of which almost all are e^+e^- pairs, are combined to form vertex candidates. The vertex position is calculated using a global χ^2 minimization algorithm [11]. Only pairs with tracks in opposite halves of the detector volume are considered.

V. EVENT SELECTION

After the data samples go through reconstruction, further event selection is required to remove background Standard Model processes and isolate potential signal events. This additional event selection was performed in two stages.

A. Preselection

The preselection cuts are designed to remove poorly reconstructed tracks and vertices as well as accidental e^+e^- pairs from the data sample, leaving pairs from tri- 323 dent and WAB events. In addition to the presence of a^{324} pair trigger, the best handle on accidental vertices are 325 strict requirements on the track and cluster times of the reconstructed particles. Additionally, well-reconstructed tracks and vertices are selected by cuts on the fit χ^2 and 326 the number of hits on track. The preselection cuts are summarized in Table I.

Each reconstructed event is then required to have ex-328 actly one of these preselected vertices. This requirement 329 mostly removes events in which no high-quality vertex330 was reconstructed; however, this selection also eliminates331 pileup backgrounds and the statistical overlap of the two332 hit-content categories defined later for tight selections. 333

The preselected data sample is used to optimize₃₃₄ the displaced vertex selection cuts, described in Sec-₃₃₅ tion VB3. The preselected MC sample is also used to₃₃₆ estimate the fraction of radiative events in the data sam-₃₃₇ ple as a function of e^+e^- invariant mass, providing a₃₃₈ reference for the expected signal yield that reduces the₃₃₉ dependence on MC modeling of experimental efficiencies₃₄₀ as described in Section VI.

Cut Description	Requirement
Trigger	Pair1
Track Time Relative to Trigger	$ t_{\rm trk} \le 6 \rm ns$
Cluster Time Difference	$\Delta(t_{\text{clu},e^-}, t_{\text{clu},e^+}) \le 1.45 \text{ns}$
Track-Cluster Time Difference	$\Delta(t_{\rm trk}, t_{\rm clu}) \le 4.0 \rm ns$
Track Quality	$\chi^2_{\rm trk}/{\rm n.d.f.} \le 20.0$
Beam Electron Cut	$p_{e^-} \le 1.75 \mathrm{GeV}$
Minimum Hits on Track	$N_{ m hits} \geq 7$
Unconstrained Vertex Quality	$\chi^2_{\rm vtx} \le 20.0$
e^+e^- Momentum Sum	$p_{\mathrm{sum}} \leq 2.4 \mathrm{GeV}$

TABLE I. Preselection requirements for e^+e^- vertex candidates.

B. Tight Selection

Following the general event selections to produce a sample of cleanly reconstructed events with e^+e^- vertices minimally impacted by pileup, a set of tight selections aimed specifically at sensitivity to the SIMPs signature is used to define the final event sample for the search.

1. Signal Kinematics Selection

In the SIMP model, the A' decays to a stable, unobserved light dark meson π_D and a heavier vector meson V_D . This shifts the signal region total momentum from near beam energy, as in the case of the nominal A' search, to significantly lower values; thus, a selection on the sum of the momentum magnitudes is applied.

$$p_{\text{sum}} = |\vec{p}_{e^-}| + |\vec{p}_{e^+}| \tag{1}$$

Specifically, the signal region (SR) used for the SIMP search requires $1.0\,\mathrm{GeV} < p_\mathrm{sum} < 1.9\,\mathrm{GeV}$ and the control region (CR) used for determining the trident differential production rate is $1.9\,\mathrm{GeV} < p_\mathrm{sum} < 2.4\,\mathrm{GeV}$.

2. Displaced Vertex Categories

The sources and characteristics of falsely displaced vertices depend upon the hit content of the tracks, and especially on the presence or absence of hits in the layers closest to the target. To enable the optimization of selections according to these attributes, the data is split into two mutually exclusive categories according to the hit content of the tracks.

The first analysis category is called "L1L1", which consists of vertices where both tracks leave hits in both sensors in the first two tracking layers (L1 and L2). These events have the best vertex resolution, although signal acceptance is limited to decays well upstream of L1, as depicted in Figure 5. Hits in L2 are required to minimize pattern recognition errors and multiple scattering contributions in projecting tracks to the vertex.

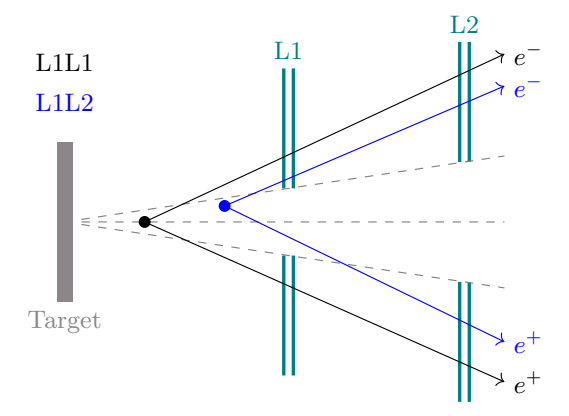


FIG. 5. Diagram showing sthe two mutually exclusive categories based on the track hit content within a vertex "L1L1" (black) and "L1L2" (blue).

342

343

344

345

346

348

349

351

352

353

354

355

356

357

359

360

362

363

364

365

366

367

368

369

370

371

373

The second analysis category is called "L1L2" and includes events where one track misses L1 due to a hit inefficiency or reduced acceptance due to longer lifetimes. Just as "L1" tracks must also have hits in L2, tracks that miss L1 are required to have hits in both L2 and L3. The L1L2 category has poorer vertex resolution and introduces more complicated backgrounds, such as an increased rate of WAB conversions coming from the L1 material.

3. Displaced Vertex Selection

The following section describes the selection procedure used to search for the displaced vertices expected in signal events. All relevant cuts are summarized in Table II.

Signal e^+e^- pairs should be reconstructed at a distance displaced from the target but consistent with a parent particle originating from the beamspot on the target. This is verified by projecting a vertex candidate back towards the target at z_{target} , using the reconstructed vertex momentum. The target-projected vertex has new coordinates x_{target} and y_{target} which can then be used to calculate a significance using the beamspot mean, $\mu_{x,y}$ and standard deviations, $\sigma_{x,y}$. The shape, size, and position of the beamspot on the target depend on the beam conditions for a given run and are therefore characterized on a run-by-run basis. The average characteristics³⁷⁵ of the beamspot are also modeled in MC, without run³⁷⁶ dependence. The vertex projection significance (VPS),³⁷⁷ as defined in Equation (2), is then required to be below³⁷⁸ some threshold in order to keep the vertex candidate:

$$VPS = \sqrt{\left(\frac{x_{\text{target}} - \mu_x}{\sigma_x}\right)^2 + \left(\frac{y_{\text{target}} - \mu_y}{\sigma_y}\right)^2} \ . \tag{2}$$

Since the strip sensors of the axial(stereo) layers of the SVT are oriented with the measurement coordinate in(near) the vertical direction, the vertical impact pa-386

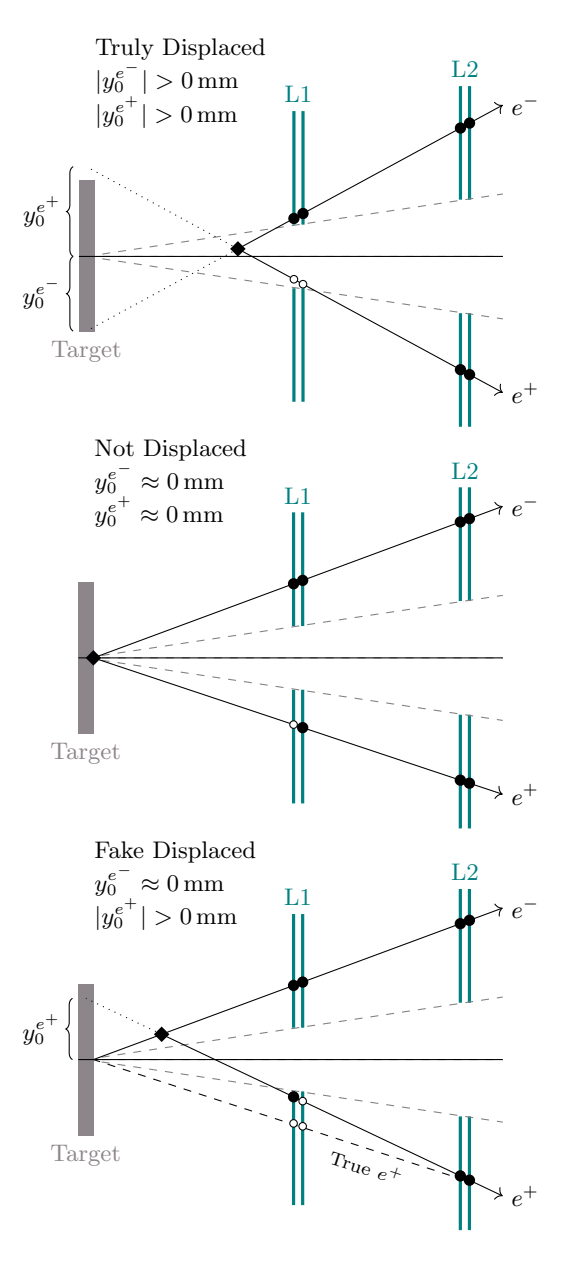


FIG. 6. Illustrations of the vertical track impact parameters y_0 at the target for truly-displaced events (top), not-displaced events (middle), and fake-displaced events (bottom) due to scattering or reconstruction errors.

rameter y_0 has higher resolution compared to the horizontal impact parameter and can be used to discriminate against falsely displaced vertices. For truly displaced signal vertices, both tracks creating the vertex typically have y_0 far from zero. In contrast, background vertices often have one prompt track correctly reconstructed with y_0 near zero, and the second track with a significant y_0 due to multiple scattering or mis-reconstruction. These scenarios are depicted in Figure 6. This motivates selecting vertices based on requiring the minimum of the two absolute y_0 values to be above a certain threshold,

$$y_{0,\min} = \min(|y_{0,e^-}|, |y_{0,e^+}|)$$
 (3)

Finally, placing an upper limit on σ_{y_0} for both tracks within a vertex removes some highly-displaced vertices arising from imprecisely measured tracks:

$$\sigma_{y_0,\text{max}} = \max(\sigma_{y_0,e^-}, \sigma_{y_0,e^+})$$
 (4)

Selection	L1L1	L1L2
Missing Energy	$1.0\mathrm{GeV} <$	$p_{\rm sum} < 1.9 {\rm GeV}$
From Beamspot	VPS < 2	VPS < 4
Lower y_0 Error	- o	$r_{y_0,\text{max}} < 0.4 \text{mm}$
Highly Displaced	$y_{0,\mathrm{min}} >$	$y_{0,\min}^{\text{cut}}(m_{\text{reco}})$

TABLE II. Summary of the final tight selection depending on hit-content category. All selection variables are explained in Section V, except for p_m which is a measure for the mass resolution, and defined in Section VI.

4. Selection Optimization

The selections for both L1L1 and L1L2 categories are optimized independently on simulated signal samples and a 10 % subsample of the collected data, representing the population of background events since no sensitivity is expected at this sample size. As described previously, the minimal vertical impact parameter $y_{0,\mathrm{min}}$ of each vertex provides high discrimination power between signal and falsely displaced background events. Therefore, we carry out our final analysis in $y_{0,\mathrm{min}}$ as a function of reconstructed vertex mass, m_{reco} . In this $(y_{0,\mathrm{min}}, m_{\mathrm{reco}})$ -space, a signal would appear as an excess of high $y_{0,\mathrm{min}}$ events at a given mass.

Except for $y_{0,\min}$, all of the selections are optimized by keeping the signal efficiency high (at least 80%) while removing background events with relatively high values of $y_{0,\min}$. While the $\sigma_{y_0,\max}$ parameter was not found to be powerful for the L1L1 category, it is helpful in removing highly-displaced background events within the L1L2 category.

Finally, the $y_{0,\rm min}$ parameter is optimized by maximizing the binomial significance of the signal yield above the remaining background. The signal yield was calculated as described in Section VIB1 and is scaled up by⁴²⁸ a factor of $0.1/\epsilon$. This is done to achieve a comparable number of signal events to the background in this sub-429 sample, which is necessary in order for the optimization algorithm to work correctly. In order to be less sensitive to statistical fluctuations and to get a smooth distribu-432 tion of $y_{0,\rm min}^{\rm cut}$ as a function of mass, the selections chosen 433 from this optimization were then fit with a second (first) 434 order polynomial for the L1L1 (L1L2) category.

Figure 7 shows the distributions of $y_{0,\min}$ as a function₄₃₆ of m_{reco} for the L1L1 and L1L2 hit-content categories₄₃₇ in data after all selections have been applied. The final $y_{0,\min}$ cut is illustrated in red for L1L1 and L1L2 events, respectively.

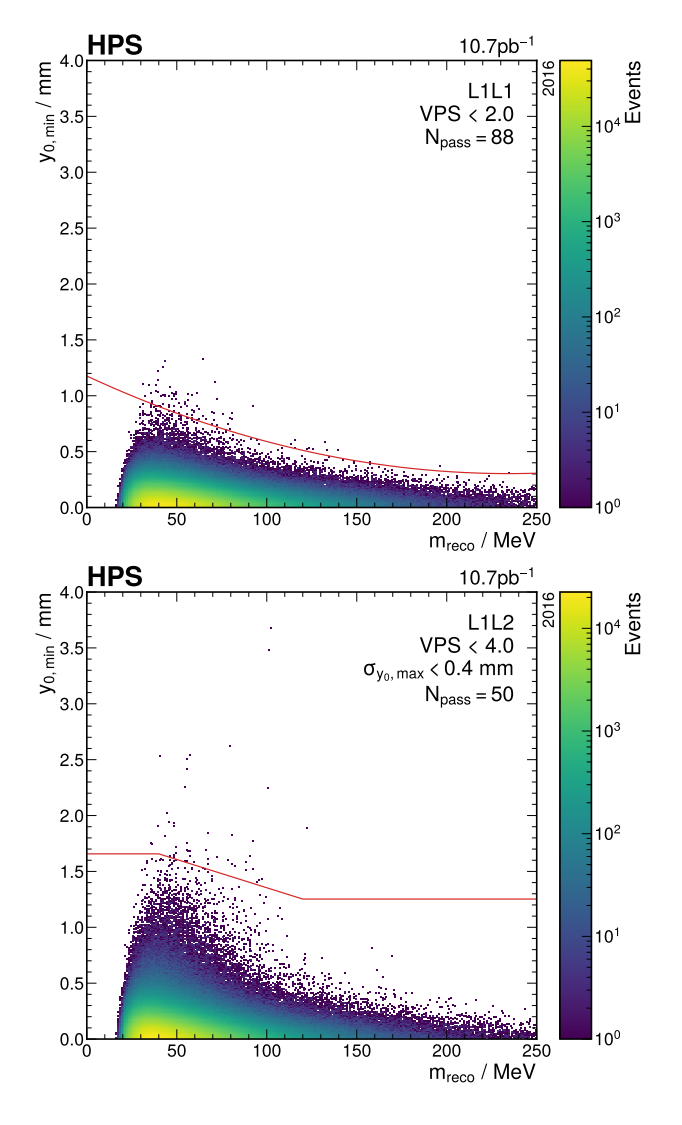


FIG. 7. $y_{0,\min}$ distribution as a function of reconstructed invariant mass m_{reco} with the final selection $y_{0,\min}^{\text{cut}}$ drawn in red for the L1L1 (L1L2) hit-content category in red on top (bottom). Here, a SIMP-like signal would appear as an excess of high $y_{0,\min}$ events – beyond $y_{0,\min}^{\text{cut}}$ – within a certain mass window. The number of events past the $y_{0,\min}$ cut, N_{pass} is noted for each category.

VI. DATA ANALYSIS

This analysis searches for an excess of events at some particular e^+e^- mass where both tracks have large values of $y_{0,\min}$, indicative of highly displaced vertices. Since we are searching for the dark vector boson V_D via its 2-body decay into e^+e^- , we expect the invariant mass of the vertex m_{reco} to be within a certain range of the mass m_{V_D} we are searching for. Since the width of the peak is dominated by the detector resolution σ_m , we expect the signal to be concentrated in a region defined by

$$p_m = \frac{|m_{\text{reco}} - m_{V_D}|}{\sigma_m} \ . \tag{5}$$

Applying an upper limit on p_m defines a mass window since it requires that $m_{\rm reco}$ resides within a small range around m_{V_D} . In this analysis, we require $p_m < 1.5$. The mass resolution dependence on invariant mass is shown in Figure 8. The mass resolution is obtained from signal MC and validated by comparing the resolution of the Møller scattering peak between MC and data.

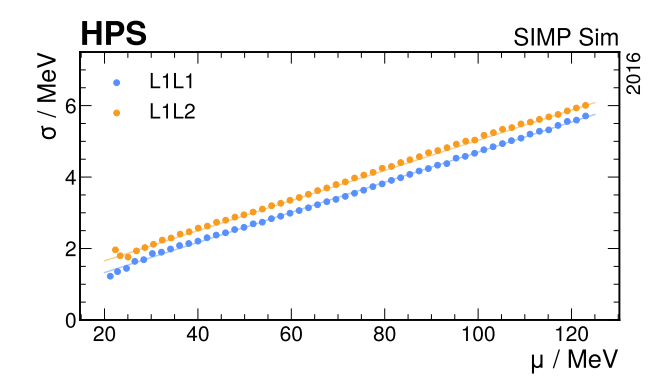


FIG. 8. The mass resolutions invariant mass as estimated from Monte Carlo at various masses of A'. The line is the result of a polynomial fit to the points and is used in the analysis.

A. Search Procedure

Before applying the final selection on $y_{0,\rm min}$, we perform a background estimation via an ABCD-like technique[12, 13] in the $(y_{0,\rm min},\,m_{\rm reco})$ -space and compare this estimate to the observation to check for a signal-like excesses. The ABCD method uses sidebands to estimate the background rate in a signal region. Choosing ranges in $m_{\rm reco}$ over which the width of the $y_{0,\rm min}$ distribution varies in a roughly linear fashion, we separate our search space into signal regions and sidebands in $m_{\rm reco}$ and $y_{0,\rm min}$. Along the $m_{\rm reco}$ axis, there are two sidebands⁴⁷⁵ – one below and one above the signal region – while there is one lower sideband along the $y_{0,\rm min}$ axis. Table III⁴⁷⁷ gives the definition of these regions and Figure 9 shows⁴⁷⁸ an example of these regions along with the calculation⁴⁷⁹ described below for the L1L1 channel.

We project the sidebands into region F to obtain the 481 expected number of events $F_{\rm exp}$ according to

$$F_{\text{exp}} = C \times \frac{\max(A + E, 0.4)}{B + D}$$
, (6)₄₈₅

where A stands for the number of events within $region_{487}$ A, B for number of events in region B, etc. The limiting₄₈₈ value of 0.4 was chosen because a Poisson mean of 0.4_{489} is the highest possible mean with zero observed counts₄₉₀ being the most probable outcome.

The statistical test for excess is performed using 10 000₄₉₂ toy counting experiments. We construct the distribution₄₉₃

Region		$y_{0,\mathrm{min}}$ Range
A	$ \begin{vmatrix} (m_{V_D} - 4.5\sigma_m, m_{V_D} - 1.5\sigma_m) \\ (m_{V_D} - 4.5\sigma_m, m_{V_D} - 1.5\sigma_m) \\ (m_{V_D} - 1.5\sigma_m, m_{V_D} + 1.5\sigma_m) \\ (m_{V_D} + 1.5\sigma_m, m_{V_D} + 4.5\sigma_m) \\ (m_{V_D} + 1.5\sigma_m, m_{V_D} + 4.5\sigma_m) \\ (m_{V_D} - 1.5\sigma_m, m_{V_D} + 1.5\sigma_m) \end{vmatrix} $	$(y_{0,\min}^{\mathrm{cut}},\infty)$
В	$(m_{V_D} - 4.5\sigma_m, m_{V_D} - 1.5\sigma_m)$	$(y_{0,\min}^{\mathrm{floor}}, y_{0,\min}^{\mathrm{cut}})$
$^{\mathrm{C}}$	$\left \left(m_{V_D} - 1.5\sigma_m, m_{V_D} + 1.5\sigma_m \right) \right $	$(y_{0,\min}^{\mathrm{floor}}, y_{0,\min}^{\mathrm{cut}})$
D	$(m_{V_D} + 1.5\sigma_m, m_{V_D} + 4.5\sigma_m)$	$(y_{0,\min}^{\mathrm{floor}}, y_{0,\min}^{\mathrm{cut}})$
\mathbf{E}	$\left \left(m_{V_D} + 1.5\sigma_m, m_{V_D} + 4.5\sigma_m \right) \right $	$(y_{0,\min}^{\mathrm{cut}},\infty)$
F	$\left \left(m_{V_D} - 1.5\sigma_m, m_{V_D} + 1.5\sigma_m \right) \right $	$(y_{0,\min}^{\mathrm{cut}},\infty)$

TABLE III. Region definitions for use in background estimation via sidebands. Region F is the signal region in which we are searching for an excess. m_{V_D} is the mass point we are searching for, σ_m is the detector mass resolution evaluated at m_{V_D} , $y_{0,\min}^{\text{cut}}$ is the optimized cut value evaluated at m_{V_D} , and $y_{0,\min}^{\text{foor}}$ is the maximum value of $y_{0,\min}$ such that region C has at least one thousand events in it.

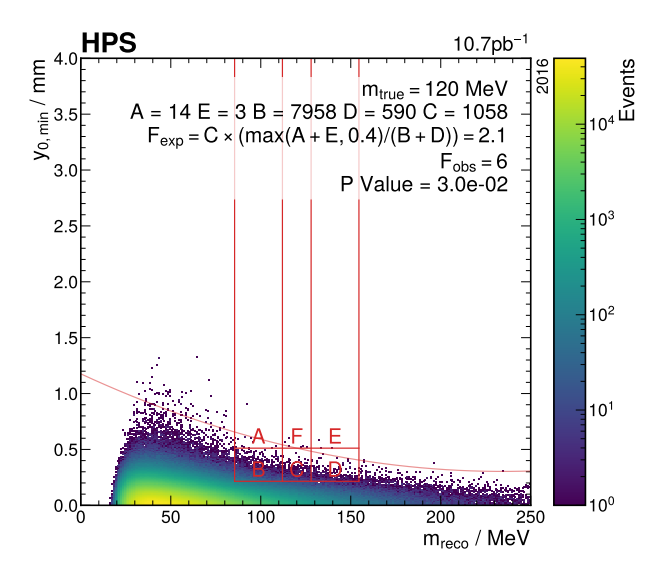


FIG. 9. Example search calculation within the L1L1 channel showing the six regions and how the calculation is performed.

of $F_{\rm exp}$ by sampling C and B+D from normal distributions and A+E from a Poisson distribution, where the means of the distributions are given by the data. This null distribution is then integrated from the observed number of events in region F up to infinity to obtain an approximate probability that the observed number aligns with the background prediction, which we use as the local p-value.

This procedure is repeated for each mass m_{V_D} in our search range, producing Figure 10 showing the comparison between expected and observed event yields in region F and their corresponding p-values derived from these toy experiments. The lowest observed p-value at $m_{\rm reco}=97\,{\rm MeV}$ achieves less than 3σ global significance, where the global significance is estimated by dividing the local significance by an approximate number of independent mass bins in which the search was performed. The excess only exists within the L1L2 category, supporting the conclusion that this is a normal (although rare) statistical fluctuation.

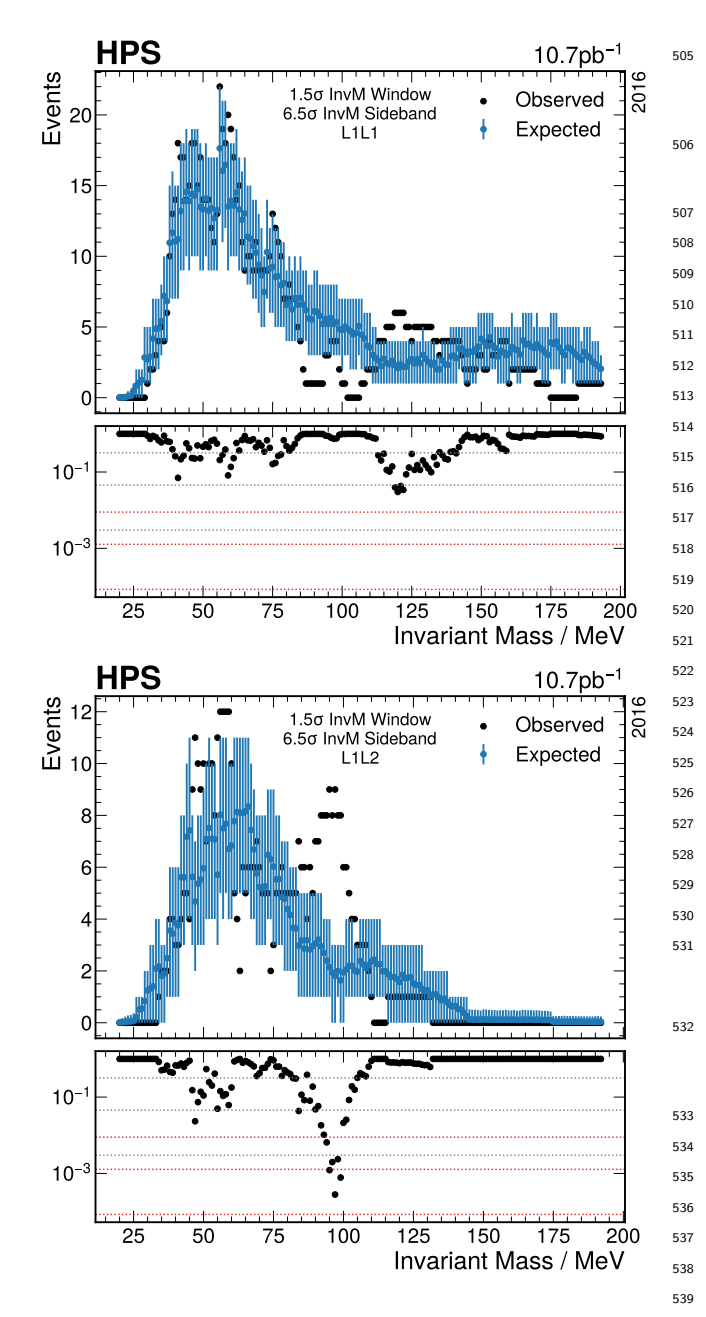


FIG. 10. Search results for the L1L1 (L1L2) hit-content category on top (bottom). The gray (red) dotted lines in the lower panels are 1σ , 2σ , and 3σ local (global) significance lines.

B. Exclusion Procedure

495

497

498

500

501

503

504

541

Without statistically sound evidence for a SIMP-like signal excess, the question can be inverted to ask what⁵⁴⁴ SIMP parameters can be excluded given the lack of ex-⁵⁴⁵ cess. This exclusion calculation is done by estimating⁵⁴⁶ the sensitivity of this analysis which is defined as the ra-⁵⁴⁷ tio of the expected signal yield to the maximum allowed⁵⁴⁸ signal yield. The maximum allowed signal yield at 90%⁵⁴⁹ confidence level is calculated using the Optimum Inter-⁵⁵⁰ val Method (OIM) [14]. We describe the expected signal⁵⁵¹

yield calculation in greater detail below.

1. Expected Signal Yield

In this signal hypothesis, we do not observe the dark photon production or decay. Instead, the dark photon decays to an unobservable dark pion and the neutral dark vector meson V_D that decays to an e^+e^- pair. The expected signal yield for a given mass and kinetic mixing strength, $N_{\rm sig}(m_{A'},\epsilon)$, is calculated with all other SIMP parameters fixed $(m_{V_D}/m_{\pi_D}=1.8, m_{A'}/m_{\pi_D}=3, \alpha_D=10^{-2}, m_{\pi_D}/f_{\pi}=4\pi)$. First, the total expected A' production rate in a given dataset, $N_{A'}(m_{A'},\epsilon)$, is calculated using the radiative trident rate, expressed in simulation-derived quantities called radiative fraction and radiative acceptance.

For the A' decay, two of the relevant modes contain neutral dark vectors, ρ_D and ϕ_D , each with their production branching ratio, $BR(A' \to \pi_D V_D)$, and lifetime, $\Gamma(V_D \to e^+e^-)$, that are a function of ϵ . Therefore, the total expected signal depends on the combined acceptance and efficiency of detecting the electron-positron pair from $\rho_D \to e^+e^-$ and $\phi_D \to e^+e^-$. Since the branching ratio and lifetimes of the dark vectors depend of the effective coupling ϵ , the acceptance \times efficiency for each vector is calculated as a function of ϵ .

The A' production cross-section for dark photons of mass $m_{A'}$ is related to the radiative trident production cross-section by [6]

$$\sigma_{A'} = \frac{3\pi m_A' \epsilon^2}{2N_{\text{eff}=1}\alpha} \frac{d\sigma_{\gamma^*}}{dm_{l^+l^-}} \bigg|_{m_{l^+l^-}=m_{A'}} . \tag{7}$$

Here, $N_{\rm eff}$ is the number of available decay products (with $N_{\rm eff}=1$ since $m_A'<2m_\mu$), α is the fine structure constant ($\alpha\approx 1/137$), and the differential cross-section is evaluated at the particular mass $m_{A'}$. Multiplying both sides of Equation (7) by the integrated luminosity gives the A' production yield given the differential radiative trident rate,

$$N_{A'}(m_{A'}, \epsilon) = \frac{3\pi m_A' \epsilon^2}{2N_{\text{eff}=1}\alpha} \frac{dN_{\gamma^*}}{dm_{A'}}$$
(8)

The differential radiative trident rate in Equation (8) is broken into three components as

$$\frac{\mathrm{d}N_{\gamma^*}}{\mathrm{d}m_{A'}} = \left(\frac{\mathrm{d}N_{\gamma^*,\mathrm{CR}}}{\mathrm{d}m_{A'}} \middle/ \frac{\mathrm{d}N_{\mathrm{CR}}}{\mathrm{d}m_{\mathrm{reco}}}\right) \left(\frac{\mathrm{d}N_{\gamma^*}}{\mathrm{d}m_{A'}} \middle/ \frac{\mathrm{d}N_{\gamma^*,\mathrm{CR}}}{\mathrm{d}m_{A'}}\right) \frac{\mathrm{d}N_{\mathrm{CR}}}{\mathrm{d}m_{\mathrm{reco}}} \quad (9)$$

The first term in Equation (9) is the radiative fraction $(f_{\rm rad}(m_{A'}))$, which measures the expected contribution of radiative tridents to the measured yield of e^+e^- pairs in the control region. The radiative fraction has a slight dependence on invariant mass as shown in the top of Figure 11. The second term is the inverse of the radiative trident acceptance \times efficiency, again in the control region, referred to as the radiative acceptance $(A_{\rm rad}(m_{A'}))$

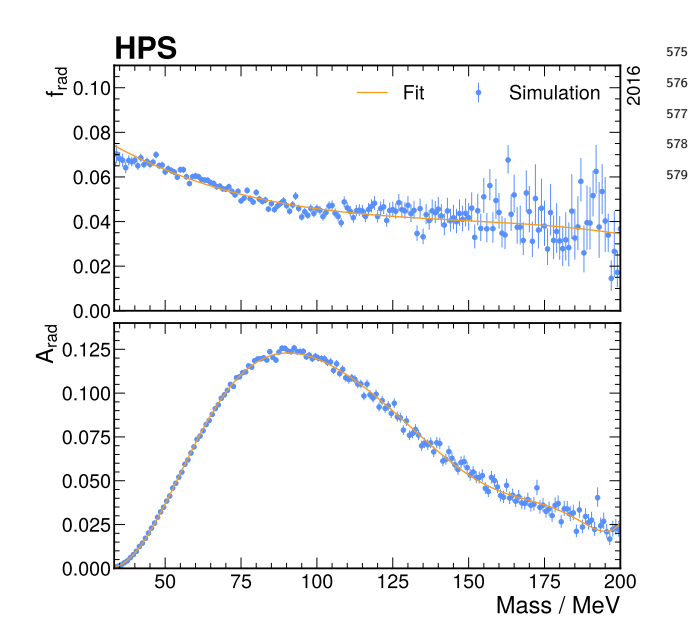


FIG. 11. The fraction (top) and acceptance×efficiency (bottom) of radiative events in our sample versus invariant mass as estimated from Monte Carlo. The lines are the plot are from polynomial fits to the points and are what are used in the analysis.

shown in the bottom of Figure 11. The third term, $\frac{\mathrm{d}N_{\mathrm{CR}}}{\mathrm{d}m_{\mathrm{reco}}}$ is the measured rate of e^+e^- pairs in the control region₅₈₃ and provides a means to scale the production rate to a₅₈₄ given dataset, whether in simulation or data.

With E(z) being the efficiency of detecting the $e^+e^-_{586}$ pair from a V_D decay and summing over the contributing dark vector mesons, the expected number of signal events can be estimated as:

$$N_{\text{sig}} = N_{A'} \int_{z_{\text{target}}}^{\infty} \sum_{V_D \in \{q_D, \phi_D\}} D_{V_D}(z) E(z) dz$$
 (10)₅₉₁

where

552

553

555

556

557

558

559

561

562

563

564

565

566

567

569

570

571

572

573

$$D_{V_D}(z) = BR(A' \to \pi_D V_D) \frac{e^{-(z - z_{\text{target}})/(\gamma c \tau_{V_D})}}{\gamma c \tau_{V_D}} \quad (11)_{5}^{5}$$

The branching ratio $BR(A' \to \pi_D V_D)$ and lifetime $\tau_{V_D}^{598}$ are taken from [5] where the lifetime explicitly depends on $m_{A'}$ and ϵ^2 . The V_D energy (and thus the relativistic ϵ_{00} γ) used in $D_{V_D}(z)$ is only distributed over a small range ϵ_{01} (within $\mathcal{O}(100\,\mathrm{MeV})$) so we replace it with the mean $\langle \gamma \rangle_{602}$ as a simplifying assumption.

2. Systematic Errors

604

606

All systematic errors arising from the experiment and $_{608}$ this analysis have been quantified individually for the two $_{609}$ hit-content categories. The systematic errors were found $_{610}$ to be within $\sim 1\,\%$ of each other for both categories. The $_{611}$ larger error of the two is used for both categories and $_{612}$

their combination. Note that some systematic effects, which would have extended reach, were not incorporated for the purpose of obtaining a conservative estimate. Table IV summarizes the systematic uncertainties which are described in this section.

Systematic	Value
radiative fraction	7 %
preselection cuts	neglected
final selection cuts	neglected
radiative acceptance	
from pre-selection	neglected
from target uncertainty	$\sim 5\%$
signal yield	
from target uncertainty	2%
from mass resolution	0.5%
beamspot	neglected
$p_{\rm sum}$ shape	$\sim 3\%$
total	$\sim 10\%$

TABLE IV. Summary of systematic errors considered and the values determined. Values marked preceded by \sim are mass-dependent and the maximum value within the most-sensitive mass range is what is listed.

The systematic error of the radiative fraction of 7% is estimated from the uncertainty on the total cross sections of the different trident processes. A detailed description of this is given in [1].

Both preselection and final cuts have systematic errors that are found to be negligible. The difference in efficiency between data and simulated trident samples is less than a few percent for the selection variables used and is lower in the simulated background than in data, so we do not correct this shift or include this systematic error. We find that the radiative acceptance is influenced most by smearing of the pre-selection cut variables and appears to be underestimated by $\sim 12\,\%$. We do not correct for this systematic shift as this would artificially improve the sensitivity since the signal yield (and therefore the sensitivity) is inversely proportional to the radiative acceptance.

The uncertainty on the target position affects both the radiative acceptance and the signal yield. To determine the resulting systematic errors, two simulated samples with the target position offset by $\pm 5\,\mathrm{mm}$ were created. This value is a conservative estimate of the uncertainty in the position of the target. From these samples, the radiative acceptance was found to be overestimated by $\sim 5\,\%$ and the signal yield was found to be overestimated by $2\,\%$ due to selections on target position-dependent variables.

The width of the beamspot and the mass resolution of the detector are underestimated within the simulation relative to the data. In order to account for this underestimate, the resulting analysis variables were smeared accordingly. This was found to have only a small effect. Due to a higher efficiency of events passing the VPS cut, the beamspot smearing improves the signal yield, so we choose to neglect it in order to keep this exclusion estimate conservative. The mass smearing, however, was found to decrease the signal yield by $0.5\,\%$ which is included in the total systematic uncertainty.

Finally, the shape of the $P_{\rm sum}$ distribution is different between data and simulated background. The effect of this systematic was determined by re-weighting events according to the ratio of the data and simulation $P_{\rm sum}$ distributions and then re-estimating the signal yield with these new weights. This led to a decrease in signal yield of $\sim 3\,\%$ for the most sensitive mass range, rising to $\sim 15\,\%$ in the lower masses.

These systematic uncertainties were summed in quadrature leading to a total of < 10% for all but the lowest mass points evaluated (rising up to $\sim 18\%$).

3. Combined Exclusion Estimates

Figure 12 shows the sensitivity for both hit-content categories for $m_{\pi_D}/f_{\pi_D}=4\pi$. The 90% confidence level exclusion contours are drawn where the sensitivity equals one after being suppressed by potential systematic errors described in the previous section. The combined sensitivity of the two categories is calculated by adding the two expected yields together and estimating the maximum allowed using the "Minimum Limit" combination technique for OIM results [15]. Figure 13 shows the resulting sensitivity along with the combined exclusion contour, including systematic errors. Compared to the individual sensitivities of the two hit-content categories, the combined result continuously covers a broader range in invariant mass and extends to $\epsilon^2 < 10^{-6}$ which neither category reaches in their own.

We also calculated the contours for $m_{\pi_D}/f_{\pi_D}=3$, a value where the decay $A'\to\pi_D\pi_D$ is roughly the same as $A'\to V_D\pi_D[5]$, but found no exclusion at 90 % confidence level.

VII. CONCLUSION

In the investigated region of the SIMP parameter⁶⁶⁸ space, couplings above $\epsilon^2 = 10^{-6}$ have been excluded⁶⁶⁹ by a reinterpretation [5] of BaBar [16] results. Our re-⁶⁷⁰ sult, given in Figure 14, contributes to this effort by con-⁶⁷¹ firming the BaBar results and probing a small portion of previously unexplored SIMP parameter space. Note that the lines shown in Figure 14 yield the current relic⁶⁷² abundance of DM for a given mass hierarchy; the chosen value of m_{π_D}/f_{π_D} yields the highest BR of visible decays⁶⁷³ [5], implying that the exclusion region for lower values⁶⁷⁴ will shrink.

A possible extension to our analysis is given by a third₆₇₆ hit category "L2L2" where both tracks miss the first₆₇₇ tracking layer. This category also suffers from complex₆₇₈ backgrounds and significantly reduced vertex resolution,₆₇₉

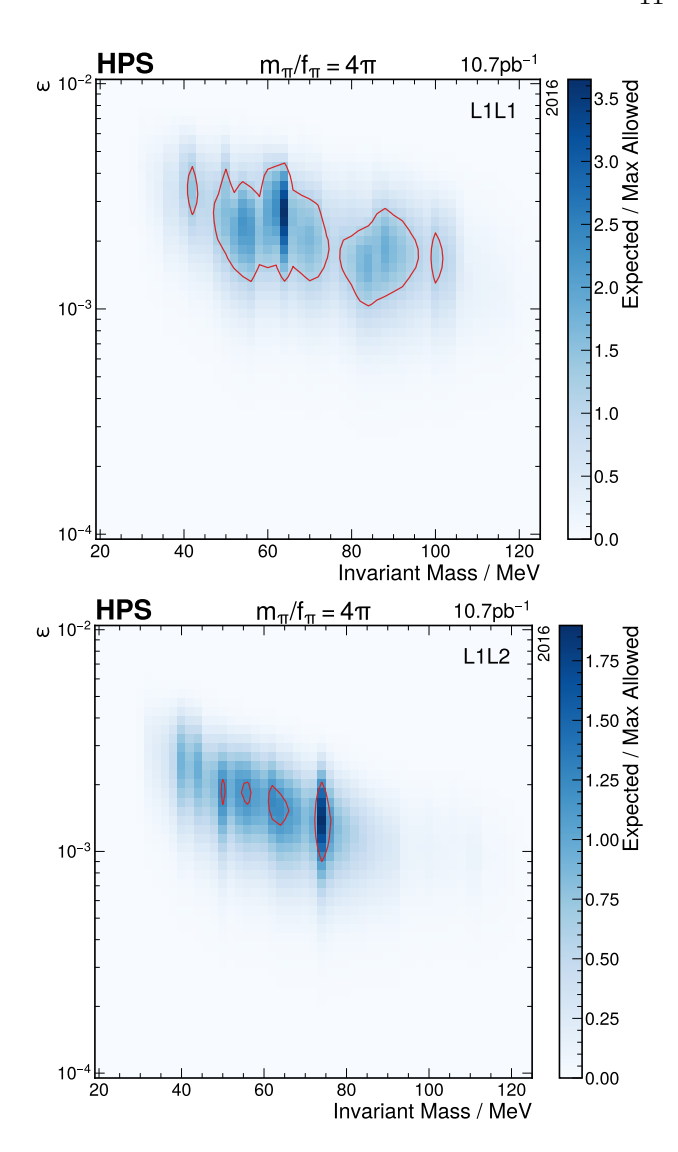


FIG. 12. Sensitivity and resulting exclusion contours for both L1L1 (top) and L1L2 (bottom) hit-content categories.

but it does have acceptance to even longer lifetimes where both tracks decay without hitting L1. The L2L2 category is particularly interesting in the context of the SIMP search because there is greater acceptance for longer decay lengths. Future analyses based on the ~ 10 times larger 2019 and 2021 data samples could include this new hit category.

VIII. ACKNOWLEDGEMENTS

The authors are grateful for the outstanding efforts of the Jefferson Laboratory Accelerator Division, the Hall B engineering group, and Forest McKinney of UC Santa Cruz in support of HPS. The research reported here is supported by the U.S. Department of Energy Office of Science, Office of Nuclear Physics; Stanford University under Contract No. DE-AC02-76SF00515 with

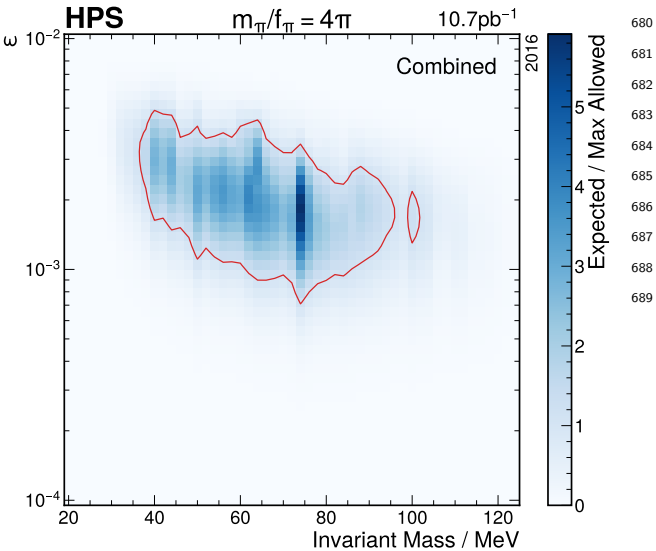


FIG. 13. Sensitivity and resulting exclusion contour for the

combination of the two hit-content categories.

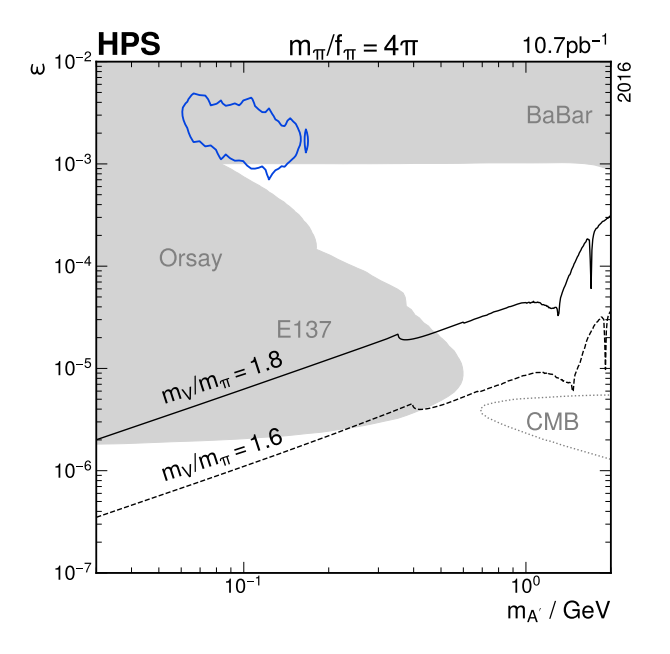


FIG. 14. Exclusion contour from this analysis with comparisons to other experiments (gray) and theoretical predictions for this model (black). [5].

690

691

692

693

694

695 696

697

the U.S. Department of Energy, Office of Science, Office of High Energy Physics; the French Centre National de la Recherche Scientifique; United Kingdom's Science and Technology Facilities Council (STFC); the Sesame project HPS@JLab funded by the French region Ile-de-France; and the Italian Istituto Nazionale di Fisica Nucleare. Jefferson Science Associates, LLC, operates the Thomas Jefferson National Accelerator Facility for the United States Department of Energy under Contract No. DE-AC05-060R23177.

^[1] P. H. Adrian et al., Searching for prompt and long-lived 698 dark photons in electroproduced e+e- pairs with the699 heavy photon search experiment at JLab, Phys. Rev. D₇₀₀ **108**, 012015 (2023), arXiv:2212.10629 [hep-ex].

P. H. Adrian et al. (HPS), Search for a dark photon₇₀₂ in electroproduced e^+e^- pairs with the Heavy Photon₇₀₃ Search experiment at JLab, Phys. Rev. D 98, 091101704 (2018), arXiv:1807.11530 [hep-ex].

^[3] Y. Hochberg, E. Kuflik, T. Volansky, and J. G. Wacker, Mechanism for thermal relic dark matter of strongly interacting massive particles, Phys. Rev. Lett. 113, 171301 (2014).

Y. Hochberg, E. Kuflik, H. Murayama, T. Volansky, and J. G. Wacker, Model for thermal relic dark matter of strongly interacting massive particles, Phys. Rev. Lett. **115**, 021301 (2015).

[5] A. Berlin, N. Blinov, S. Gori, P. Schuster, and N. Toro,726 Cosmology and accelerator tests of strongly interact-727 ing dark matter, Physical Review D 97, 10.1103/phys-728 revd.97.055033 (2018).

706

707

708

709

710

711

712

713

714

715

716

717

718

719

720

721

722

723

724

725

- [6] J. D. Bjorken, R. Essig, P. Schuster, and N. Toro, New₇₃₀ fixed-target experiments to search for dark gauge forces,₇₃₁ Phys. Rev. D 80, 075018 (2009).
- [7] C. Leemann, D. Douglas, and G. Krafft, The Continu-733 ous Electron Beam Accelerator Facility: CEBAF at the734 Jefferson Laboratory, Ann. Rev. Nucl. Part. Sci. 51, 413735 (2001).
- [8] J. Alwall et al., The automated computation of tree-levelrss and next-to-leading order differential cross sections, andrss their matching to parton shower simulations, Journal ofrss High Energy Physics 2014, 79 (2014).
- [9] H. Hirayama, Y. Namito, A. F. Bielajew, S. J. Wilder-741 man, and W. R. Nelson, The EGS5 code system, SLAC-742 R-730, KEK-2005-8, KEK-REPORT-2005-8 (2005).
- [10] S. Agostinelli et al. (GEANT4), GEANT4-a simulation toolkit, Nucl. Instrum. Meth. A 506, 250 (2003).

- [11] P. Billoir and S. Qian, Fast vertex fitting with a local parametrization of tracks, Nucl. Inst. Methods A 311, 139 (1992).
- [12] F. Abe *et al.* (CDF), A Measurement of $\sigma B(W \to e\nu)$ and $\sigma B(Z^0 \to e^+e^-)$ in $\bar{p}p$ collisions at $\sqrt{s} = 1800$ GeV, Phys. Rev. D **44**, 29 (1991).
- [13] S. Abachi *et al.* (D0), Search for high mass top quark production in $p\bar{p}$ collisions at $\sqrt{s} = 1.8$ TeV, Phys. Rev. Lett. **74**, 2422 (1995), arXiv:hep-ex/9411001.
- [14] S. Yellin, Finding an upper limit in the presence of an unknown background, Phys. Rev. D 66, 032005 (2002).
- [15] S. Yellin, Some ways of combining optimum interval upper limits (2011), arXiv:1105.2928 [physics.data-an].
- [16] J. P. Lees et al. (BaBar), Search for Invisible Decays of a Dark Photon Produced in e+e- Collisions at BaBar, Physical Review Letters 119, 10.1103/physrevlett.119.131804 (2017).